Title

Melting Point Depression and Phase Identification of Sugar Alcohols Encapsulated in ZIF Nanopores

Journal

The Journal of Physical Chemistry C, 125(18)

ISSN

1932-7447

Authors

Kang, Hyungmook
Dames, Chris
Urban, Jeffrey J

Publication Date

2021-05-13

DOI

10.1021/acs.jpcc.1c00514

Peer reviewed

Melting Point Depression and Phase Identification of Sugar Alcohols Encapsulated in ZIF Nanopores

Hyungmook Kang[1,2], Chris Dames[1]*, Jeffrey J. Urban[2]*

[1] Department of Mechanical Engineering, University of California, Berkeley, CA, 94720, USA.
[2] The Molecular Foundry, Lawrence Berkeley National Laboratory, Berkeley, CA, 94720, USA.
* Corresponding authors: cdames@berkeley.edu (C. Dames), jjurban@lbl.gov (J. J. Urban)

Abstract

Sugar alcohols (SAs) have attractive characteristics as phase change materials, but their relatively high melting temperature limits their application in the real world. Nanoconfinement can be a useful parameter to reduce the melting temperature to pragmatic ranges. Using molecular dynamics simulations, we investigate the phases and behaviors of encapsulated SA in ZIF-8 and ZIF-11, which cannot be experimentally observed. Based on reliable partial charges for the ZIF structures calculated by a density functional theory, structural analysis shows the SA's attractive interaction to the ZIF structure frustrates the SAs crystallization, and also elucidates the second-order phase transition between amorphous phases. A methodology is suggested to determine the phase transition temperature of confined materials, and used to quantify the melting temperature depression of the ZIF-confined SAs. We also explored the thermal conductivity of the SA-in-ZIF composites. Phonon frequency analysis verifies that the presence of SA molecules enhances the heat transfer by adding heat pathways between the nanoporous structure of ZIFs.

Introduction

Phase change materials (PCMs) have been widely investigated to store and release thermal energy in the form of latent heat from a phase transition. Thermal energy storage based on latent heat is one of the most efficient methods for pursuing high storage density in a small temperature range.[1-3] PCMs have been integrated into the fields of solar-thermal energy storage, pumped coolants, waste heat recovery, and off-peak electricity storage systems.[4-9] Nevertheless, the widespread utilization of PCM is limited since there is no ideal material for each specific application.[10]

In particular, the issue of building space heating by thermal energy storage has lacked appropriate PCMs with a desired melting temperature and heat of fusion, in contrast to ice storage air conditioning which can take advantage of the large latent heat of water. Traditionally, paraffin waxes and salt hydrates are commonly used for the heating and cooling energy demand in buildings.[11] Paraffin is chemically stable, and compositionally tunable to achieve a suitable melting temperature. However, paraffin shows poor thermal properties such as relatively low latent heat (Δh_L<200 Jg^{-1}), low thermal conductivity, and flammability.[12] On the other hand, inorganic salt hydrates have issues of large volume change in phase transition, corrosiveness and phase separation in spite of their good thermal properties (Δh_L~200-300 Jg^{-1}).[13] Sugar alcohols (SAs) have attractive characteristics for thermal energy storage applications.[10] SAs display a high latent heat (Δh_L>300 Jg^{-1}) and are chemically stable, non-corrosive, non-toxic and even inexpensive.[14] However, a major challenge limiting their application in the real world is their relatively high melting temperature (T_m >100 ^oC).

Recent studies have shown the confinement of PCMs at the nanoscale to improve thermo-physical properties with a versatile strategy.[3] Metal-organic frameworks (MOFs), which is an emerging class of three-dimensional porous crystalline materials, is a promising architecture because it offers nanoconfinement with high internal porosity, large surface area, and stability even at high temperatures.[15] Furthermore, the nanoconfinement can be a parameter to reduce the phase transition temperature of PCMs. For example, the decrease of the phase

transition temperature of polyethylene glycol (PEG) has been observed when incorporated into graphene oxide,[16] nanochannels of porous coordination polymers (PCPs)[17], and carbonized MOFs.[18] Recently, our group experimentally demonstrated the first encapsulation of SAs (erythritol and xylitol) within a class of MOF without an infusion process at room temperature.[19] The nanoconfinement of the sugar alcohols was found to lower the melting point of the SAs into the operating range for water cooling applications. However, the mechanism behind the observed melting point depression and the phase identification in the nanopores is currently unknown.

In this study, we investigate the phases of nanoconfined SAs using molecular dynamics (MD) simulations. Despite the observation of thermal transitions of the SA-in-MOF system by differential scanning calorimetry (DSC),[19] the structural difference between the phases consisting of a few number of SA molecules in the nanopores was not explained. Due to the few-nm length scales being too small, and lack of experimental access to a MOF pore interior, it is impossible to experimentally observe behaviors of the nanoconfined SAs. Instead, a theoretical atomistic-level approach presents guidance for synthesis and composite design.

The encapsulated SAs of the previous study were simultaneously synthesized with the building blocks of a uniformly porous structure of a zeolitic imidazolate framework (ZIF) type MOF. The ZIF structure was identified as ZIF-L. ZIF-L is a two-dimensional layered ZIF structure that is made up of the same building blocks as ZIF-8. ZIF-L is a metastable phase and would transform to ZIF-8 under organic solvent interactions with 60-80 ^{o}C temperature conditions.[20, 21] The layered structure of ZIF-L has a smaller pore size and weaker crystallinity than ZIF-8, so ZIF-8 is expected to be more suitable to contain the SAs as phase change materials. Therefore, here we select ZIF-8 and additionally ZIF-11 with a larger pore size as the frameworks to encapsulate sugar alcohols. ZIF-8 and ZIF-11 are both popular for their thermal and chemical stabilities, and the small aperture diameter of the channels between pores in normal conditions.[22]

We further explore the thermal conductivity of the SA-infused ZIFs. The thermal conductivity, k, of ZIF-11 and the SA-ZIF composites has never been measured or calculated, to

the best of our knowledge. ZIF is basically a low-*k* dielectric material. The thermal conductivity of ZIF-8 was measured (0.326 $Wm^{-1}K^{-1}$)[23] in air at the standard 1 atm and 300 K which is one order of magnitude lower than other nanoporous crystals such as zeolites sodalite (3.5 $Wm^{-1}K^{-1}$), zeolite-A (1.7 $Wm^{-1}K^{-1}$),[24] and amorphous silica (1.4 $Wm^{-1}K^{-1}$).[25] Such low *k* could be a critical issue when applying the composites into energy storage systems or as components of thermal circuits. Here we resolve the open question on whether the presence of SA molecules increases the composite k by adding additional heat pathways, or reduces it by introducing a new phonon scattering source.[26]

Model and Method

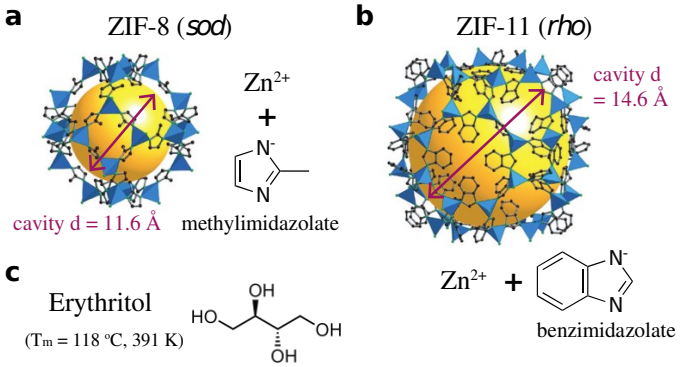

Figure 1. Structure of (a) pristine ZIF-8 (*sod*, lattice constant, a=b=c=16.99 Å) and (b) ZIF-11 (*rho*, lattice constant, a=b=c=28.76 Å), both functioning as frameworks,[22] and (c) erythritol as the phase change material. For each ZIF structure, Zn ions are represented as tetrahedra and the largest cavity in the pores by a yellow sphere that fits into the framework without touching any atoms. H atoms are omitted here for clarity but were included in the MD simulations. *Copyright (2006) National Academy of Sciences, U.S.A.*

We select ZIF-8 and ZIF-11 as the frameworks for encapsulating sugar alcohols (Fig. 1). They are suitable for this encapsulation because their rather large pore size (ZIF-8: 11.6 Å, ZIF-11: 14.6 Å) holds more SA molecules while the small inter-pore aperture diameter (ZIF-8: 3.4 Å, ZIF-11: 3.0 Å) prevents diffusion between pores.[22] In addition, the ZIFs have the same

tetrahedrally-coordinated transition metal ion, Zn(II), and similar imidazolate linkers, meaning they have similar internal surface interactions.

For the MD simulation of this system, the all-atom AMBER force fields for potential energy U are used:

$$U_{potential}=\sum_{i>j}\left[4\varepsilon_{ij}\left\{\left(\frac{\sigma_{ij}}{r_{ij}}\right)^{12}-\left(\frac{\sigma_{ij}}{r_{ij}}\right)^{6}\right\}+\frac{q_i q_j}{4\pi\varepsilon_o\varepsilon_r r_{ij}}\right]+\sum_{bonds}K_r\left(r-r_o\right)^2+\sum_{angles}K_\theta\left(\theta-\theta_o\right)^2+\sum_{torsions}\frac{K_\phi}{2}\left\{1+\cos\left(n\phi-\gamma\right)\right\}+\sum_{impropet}$$

(1)

The first term describes the non-bonded interactions including Van der Waals as the Lennard-Jones 12-6 form and Coulombic forces from atom-centered partial charges q; this includes interactions between SAs and ZIF and among different SA molecules. The next terms in Eq. (1) represent, respectively, bond stretching, bond bending, and proper and improper torsional interactions. We apply a force field developed for ZIF-8 with structural flexibility[27] to both ZIFs since they share mostly the same bonded interactions of stretching, bending, and torsion. However, to the best of our best knowledge, the partial charges for ZIF-11 have not been studied with a reliable treatment, so here we first calculated them using a density functional theory simulation with DDEC6 methodology.[28] To unify the partial charge methodology for both ZIFs, the partial charges of ZIF-8 are also calculated with the same method. The details of the force field parameters and partial charges for the ZIF-8 and ZIF-11 are summarized in Tables S1 and S2, respectively.

Regarding sugar alcohols, this study focuses on erythritol as a representative of sugar alcohols having hydroxyl (OH) groups. The thermodynamic properties of sugar alcohols are substantially affected by the OH group which forms strong intermolecular hydrogen bonds.[29] Bulk erythritol has an outstanding heat of fusion (Δh_m=337 Jg^{-1}) among sugar alcohols and a melting point (T_m=118 ^oC, 391 K)[30] not too far from the liquid water working range. The short carbon chain is also suitable for being confined in the nanopores of a ZIF. We use force field

parameters for erythritol which were used in a previous MD analysis of C6 sugar alcohols[29] and the details are summarized in Table S3.

MD simulation is performed using the LAMMPS package[31, 32] with standard 3D periodic boundary conditions. The non-bonded interactions are cut off at 12 Å while the Ewald summation method is applied to treat the long-range electrostatic interactions. The VdW interaction parameters between unlike atoms were obtained by the Lorentz–Berthelot combining rule. The non-bonded interactions separated by exactly three consecutive bonds (1–4 interactions) are reduced by related scaling factors which are optimized as 0.50 for VdW interactions and 0.83 for electrostatic interactions, respectively.[33, 34] For the upcoming investigation of the structure and melting temperature of the SA-ZIF composites (shown later in Fig. 5), the Nose-Hoover thermostat and barostat[35] is applied to the ZIF structures. All simulations are carried out at atmospheric pressure. The erythritol molecules are initially placed with an original crystal structure in the pores. After initial relaxation and equilibration, at least 3 ns of simulation is performed for each temperature condition with a fixed time step of 1.0 fs. Data from multiple cycles of increasing and decreasing temperature are collected to check and exclude a hysteresis. The next temperature varying cases start from the final state of last simulations, which means that the erythritol molecule placements at the start of subsequent simulations are thermally randomized. The simulation results are found to be hysteresis free and repeatable across multiple cycles, which confirms that the results are independent of the initial conditions. The simulation system sizes are summarized in Tables 1 and 2, where the notation "*n*pP" means "*n* erythritol molecules per pore."

Table 1. Simulation system size for the encapsulated erythritol in ZIF-8.

	case	supercell size	ZIF atoms	# of erythritol per pore	total # of erythritol[a]	erythritol atoms	total atoms
ZIF-8	pristine	2 x 2 x 2	2208	-	-	-	2208
	3pP			3	48	864	3072
	4pP			4	64	1152	3360
	5pP			5	80	1440	3648
	6pP			6	96	1728	3936

[a] A ZIF-8 (sod) unit cell has two pores, like a BCC structure.

Table 2. Simulation system size for the encapsulated erythritol in ZIF-11.

	case	supercell size	ZIF atoms	# of erythritol per pore	total # of erythritol[a]	erythritol atoms	total atoms
ZIF-11	pristine	1 x 1 x 2	2784	-	-	-	2784
	4pP			4	16	288	3072
	8pP			8	32	576	3360
	12pP			12	48	864	3648
	16pP			16	64	1152	3936
	20pP			20	80	1440	4224

[a] A ZIF-11 (rho) unit cell has two pores, like a BCC structure.

Results and Discussion

Structure of ZIFs containing erythritol

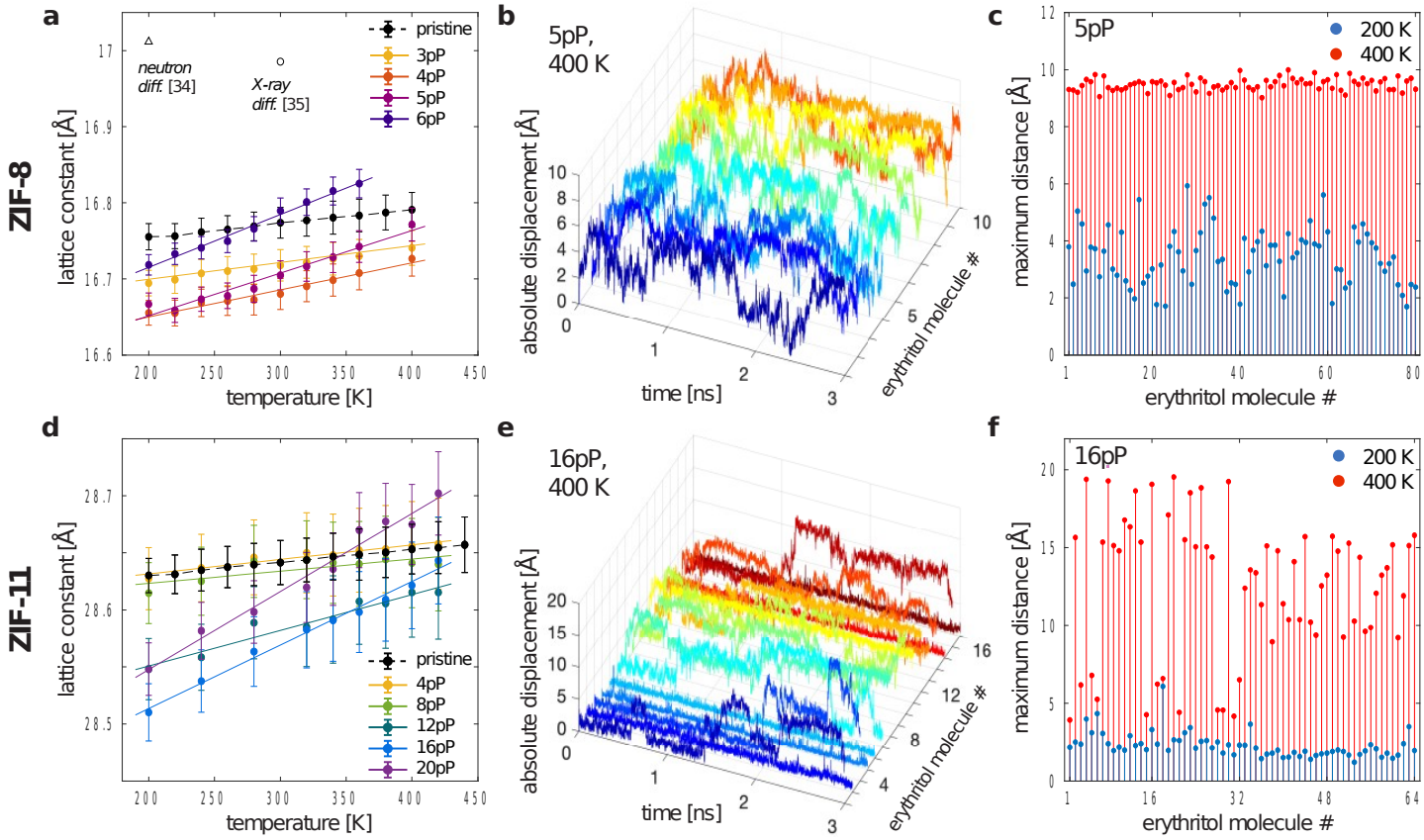

Figure 2. Structural analysis of ZIF-8 (top row) and ZIF-11 (bottom row) containing various numbers of erythritol molecules. (a,d) Effect on lattice constant according to the number of erythritol molecules per pore. (b,e) Absolute displacement (center of mass) of erythritol molecules from an origin time. Only a representative subset of molecular trajectories (10 in b, 16 in e) is shown here for visibility. (c,f) Accessible internal cavity size as determined by the maximum distance among trajectories of each erythritol molecule.

We first analyze the structural characteristics of ZIFs containing erythritol molecules (Fig. 2). The applied force field renders the lattice constant of ZIF-8 comparable with available experimental data[36, 37] within 2%, as shown in Fig. 2a. Upon beginning to add SAs into the ZIF pores, Fig. 2a shows that the lattice constant of the ZIF composites reduces, which is due to the attractive interaction between the ZIF structure and SA molecules, and between the SA molecules themselves. However, above a certain number of erythritol molecules in a pore, the

lattice constant begins to expand, due to the limitation of physical pore size. For example, this constraint effect is seen in Fig. 2a for 5 and 6 molecules per pore. Similarly, for ZIF-8 with 5 and especially 6 erythritol molecules per pore (6pP), the thermal expansion trend is different from the pristine ZIF-8 case and few-pP cases, indicating that the thermal expansion of the composite is dominated by the thermal expansion of the erythritol molecules (The volumetric coefficient of thermal expansion, α_V of ZIF-8[38] is 11.9 MK^{-1} smaller than that of solid and liquid erythritol,[30] 29.4 MK^{-1} and 395 MK^{-1}, respectively). For ZIF-11 (Fig. 2d), although shrinking of the framework size is not observed in the small quantity cases (4pP and 8pP) due to the larger pore size having enough empty space, further increasing the number of erythritol molecules gives the same trends as seen for the ZIF-8 composites in Fig. 2a.

Note that the lattice constants of 6pP in ZIF-8 and 20pP in ZIF-11 exceed that of pristine ZIFs in the temperature range of our interest (< 400 K), which has the potential to break the ZIF structures in a real application. Therefore, we conclude that ZIF-8 and ZIF-11 safely contain up to 5 and 16 erythritol molecules per pore, respectively. Then, in order to check the extent of diffusion between pores, we track the absolute displacement of every erythritol molecule from their respective origins at the highest loading conditions, and present representative results of a subset of molecules in Figs. 2b and 2e. As expected, based on the small inter-pore aperture diameter of the ZIFs, the absolute displacement does not exceed a certain distance, which means that erythritol molecules move around only within their original pore. Figures 2c and 2f show the maximum distance of every erythritol molecule itself during their 3 ns trajectory. ZIF-8 and ZIF-11 have the allowable cavity distance for erythritol as around 10 Å and 20 Å, respectively. The latter is larger than the nominal inner spherical cavity diameter of d=14.6 Å indicated in Fig. 1, but this is reasonable since the accessible spherical cavity diameter is somewhat larger due to the free space in between the benzimidazolate molecules. Furthermore, we notice from Figs. 2c and 2f that the encapsulated erythritols at low temperatures (200 K) are no longer mobile but rather vibrate locally within a ~3-5 Å range. The distinction between these two phases (the mobile, liquid-like, high-temperature phase; and the immobile, low-temperature phase) will be discussed further below.

Structure of encapsulated erythritols

The radial distribution function (RDF), *g(r)*, is used to understand structural features of the encapsulated erythritol molecules. The g(r) is defined as

$$g(r)=\frac{dn(r)}{\rho_n 4\pi r^2 dr} \quad (2)$$

Where *n(r)* is the number of particles within a shell of thickness dr and ρ_n is the average number density of the particles in each simulation system. Figure 3 explains the erythritol structure by the RDFs of two significant atomic relations through comparisons with that of the solid and liquid state of pure erythritol from additional simulations. First, the mid-carbon (CT_m) atoms are taken as the central reference site showing the general density distribution. Figures 3a and 3c show that the RDFs between CT_m of the encapsulated erythritol are similar to the RDFs of the liquid state of pure erythritol, i.e. relatively slowly varying *g(r)* with few peaks, for the entire temperature range, in spite of the initially placed crystal structure of erythritol. Hydrogen bonds among their OH groups are also the key interaction that attracts SA molecules to each other. The major difference between pure crystal and liquid erythritol is the hydrogen bond between terminal-oxygen (O_t) atoms and mid-hydrogen (HO_m) atoms. For the crystalline structure, the combination of O_t and HO_m hardly constitutes hydrogen bonds, which would show up as a strong first peak at around 2 Å on the RDF graph between O and H. On the other hand, the amorphous liquid state does form hydrogen bonds and its RDF between O_t and HO_m (black dashed lines in Figs. 3b and 3d) shows a strong peak at 2 Å. The encapsulated erythritol O_t-HO_m RDF results show a similar strong peak around 2 Å and other similar RDF features as pure erythritol liquid. Therefore, we conclude that the nano-confinement with the boundary attractive interaction between SAs and the ZIFs frustrates the SA crystallization and causes them to remain in an amorphous structure.

Nevertheless, we can notice some evidence that there are two distinguishing amorphous phases from the RDF graphs. At the lower temperatures of Fig. 3 there are some signatures of the beginning of ordering. The first peak (around 5.5 Å) of the CT_m RDF splits and the movement of secondary peaks (the range of 3 to 5 Å) of the RDF between O_t and HO_m are observed at the low-temperature range. The melting temperature (T_m) of encapsulated erythritol is definitely reduced from the original melting temperature (of 391 K), and the depression amount for the encapsulation with ZIF-8 is larger than with ZIF-11 due to the stronger interaction by the smaller pore size.

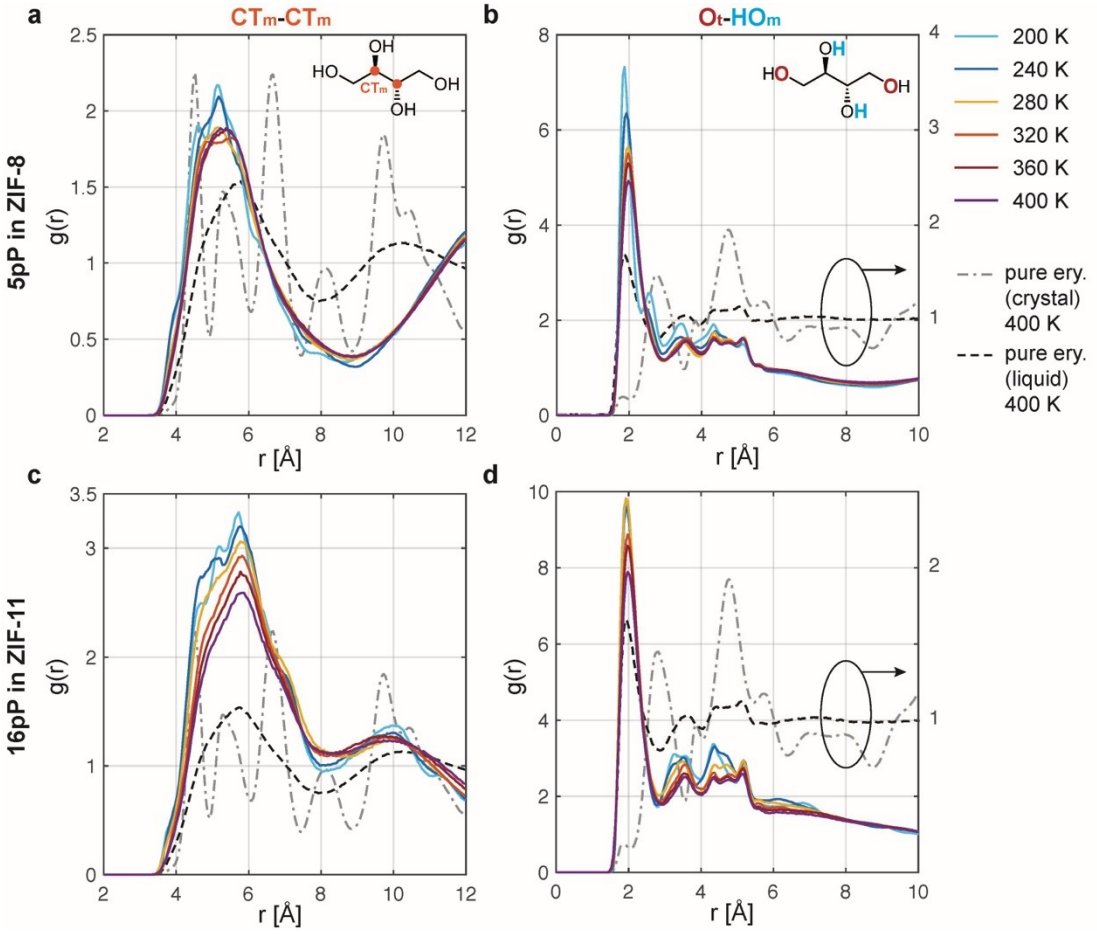

Figure 3. Radial distribution function among erythritol molecules inside ZIF-8 (top row) and ZIF-11 (bottom row). (a,c) RDF between the mid-carbon (CT_m) atoms. (b,d) RDF between terminal-oxygen (O_t) atoms and mid-hydrogen (HO_m) atoms

Melting temperature of encapsulated erythritols

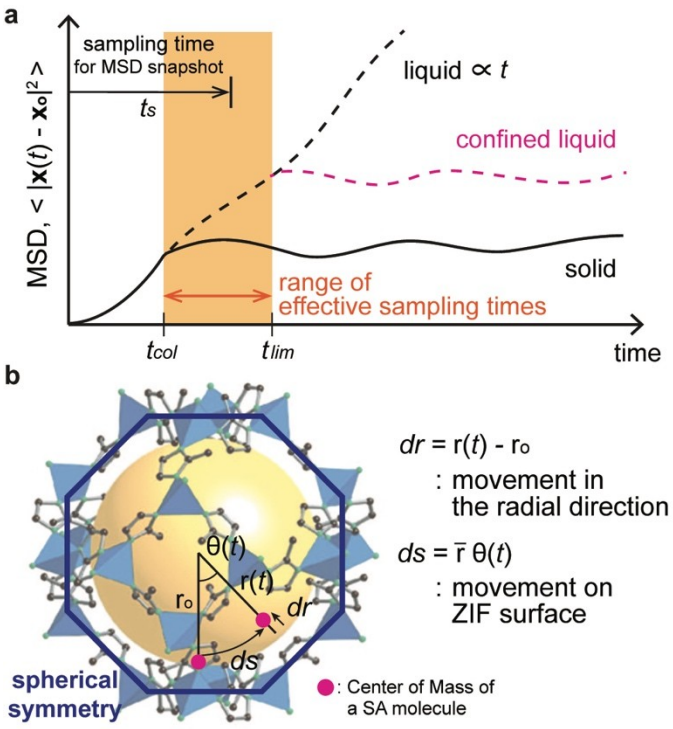

Figure 4. Mean squared displacement. (a) Conceptual examples of two idealized systems (bulk liquid, bulk solid) and the confined liquid system. (b) The split of movement of an SA molecule into circumferential (*ds*) and radial (*dr*) directions based on the spherical symmetry of a ZIF pore.

Melting temperature T_m is one of the most important and interesting properties for the composites. Although the depression of T_m was observed from the RDF analysis, determining T_m with a higher accuracy is required to understand further the amorphous phases. Many methods in MD simulation have been developed for the computation of T_m: the hysteresis method, the voids method, and the solid-liquid interface method as direct methods; and the free energy methods as indirect methods.[39] However, those direct methods are not suitable for materials with a small number of atoms/molecules and the indirect methods require a clear understanding of the two reference phases. In order to figure out the T_m of the nanoconfined erythritols, we here take a different approach, beginning with the fundamentals of particle diffusion. The mean squared displacement (MSD) has been generally used to measure a diffusion coefficient:

$$MSD \equiv \left\langle \left| x(t) - x_0 \right|^2 \right\rangle = \frac{1}{N} \sum_{i=1}^{N} \left| x^{(i)}(t) - x^{(i)}(0) \right|^2, \quad (3)$$

where N is the number of particles in simulation system, vector $\mathbf{x}^{(i)}(t)$ is the position of the i-th particle at time t, and $\mathbf{x}^{(i)}(0) = \mathbf{x_0}^{(i)}$ is the reference position of the i-th particle. Figure 4a presents the trends of MSD of two idealized systems (bulk liquid, bulk solid) as well as the system considered here in which a liquid is confined to a small fixed volume. For identification of bulk phases, it would be straightforward to distinguish liquid from solid phases from an MSD(t) calculation accordingly, by looking for either MSD increasing linearly with t or saturating with t.

However, in the confined systems, the MSD saturates for the liquid phase as well as the solid phase. Such a saturated long-time MSD(t) behavior was confirmed in our systems at all temperatures considered (Fig. S1). Nevertheless, theoretically the difference between the solid-like and liquid-like phases in the confined volume can still be observed in a shorter effective sampling time range (highlighted as the orange color in Fig. 4a) after the collision time, t_{col}, and before the time limit, t_{lim}, which scales with the accessible cavity size (~d of Fig. 1). To calculate the MSD we analyze a snapshot of the simulation at some sample time, t_s, which must be chosen carefully. If t_s is too short, i.e. $t_s < t_{col}$, even liquid phases will not have had enough time for their molecules to diffuse around significantly, and the MSD of liquid and solid phases will be indistinguishable. Then for a range of $t_s > t_{col}$, the MSD(t) curves for solid and confined liquid phases will diverge: the solid phase MSD(t) saturates for $t_s > t_{col}$ while the confined-liquid phase MSD(t) will continue increasing. Finally, if t t_s is too large, i.e. $t_s > t_{lim}$, the confined-liquid's MSD(t) will also saturate due to the finite pore confinement volume. Thus, the best regime for distinguishing solid from confined-liquid phases based on their different MSD(t) slopes is the orange zone in the figure. Below the movements of the erythritol molecules are analyzed by dividing them into tangential and perpendicular movement to the ZIF surface. The *sod* structure of ZIF-8 and *rho* structure of ZIF-11 are approximately spherically symmetric, so the MSD can be expressed by the movement in the radial direction and on the ZIF surface, *dr* and *ds*, with the convenience of spherical coordinates as detailed in Fig. 4b.

We consider 5 sampling times, t_s=0.5 ps, 1.0 ps, 1.5 ps, 2.0 ps and 2.5 ps, to identify the phases and t_{col}. The results of the snapshotted MSD at the 5 prescribed sampling times are summarized in Fig. 5. To better compare the 2d movement of *ds* vs. the 1d movement of *dr* on the same footing, we choose to plot $(ds^2)/2$ in the figure. Figure 5 reveals several phenomena. First, in all of the cases tested the movement of the SA molecules along the ZIF surface is equal to or larger than movements in the radial direction, i.e. $(ds^2)/2 \geq dr^2$, with the largest differences occurring at high temperature and in the ZIF-8 whose pore size is smaller. Since the interaction between erythritol and ZIFs is attractive as observed above, the perpendicular movement of erythritol away from the pore surface (*dr*) is limited, like adsorbates on a 2d substrate; while circumferential diffusion (*ds*) while still adsorbed to the pore surface is relatively easier. This phenomenon is exaggerated in ZIF-8 rather than ZIF-11, since in the latter some erythritol molecules can be located without adjacent interaction with the pore surface due to the larger pore size. Thus, we determine the collision time, t_{col}, by focusing on the MSD(*t*) results of the dominant movement, ds^2. At temperatures low enough that the SA molecules can be considered as a solid-like phase, the MSD evaluated at sampling times $t_s > t_{col}$ should converge and saturate as explained in Fig. 4a.

Although t_{col} is dependent on the temperature and the number density, here we suggest a practical way to define T_m with an example of Fig. 5c. The ds^2 at T=360 K clearly keeps increasing with t_s, reminiscent of the effective range ($t_{col} < t_s < t_{lim}$, the orange regime of Fig. 4a), and thus we identify this behavior as confined liquid-like phase. On the other hand, the 280 K data of Fig. 5c shows that ds^2 basically saturates for $t_s \geq 1.0$ ps, and we identify this as solid-like phase, with $t_{col} < 1.0$ ps. The transition between these two behaviors is thus identified as the melting temperature, T_m, and indicated by the vertical dashed red line at around 305 K in Fig. 5c(bottom). The same T_m analysis to assess whether ds^2 keeps increasing with $t_s > t_{col}$, or saturates, is applied to the other panels as indicated by their respective dashed red lines.

Like the simple observation in Fig. 3, the analysis in Fig. 5 also shows T_m of erythritol is reduced by the encapsulation in nanopores from the original bulk T_m of 391 K. The T_m

depression is stronger for smaller pore sizes and smaller number of SA pP. Although Fig. 5 shows the movements of SA along the ZIF surface dominate those normal to it ($ds>dr$) due to the attractive interaction between SA and ZIF, there are no hydrogen donor or acceptor sites in the ligands of ZIF structures. The RDFs between erythritol and ZIFs also support the absence of hydrogen bonds (Figs. S2 and S3). The latent heat of bulk SAs mainly originates from the changes in the hydrogen bond network. Compared to the first-order phase transition of pure erythritol with its strong hydrogen bonds, the required kinetic energy for the second-order phase transition between amorphous phases of encapsulated SA is relatively lower; this also reduces the T_m. The balance between the hydrogen bonding interaction among SAs and the effect from attractive potential field of ZIF surface can also be understood through the surface-to-volume ratio. As more erythritol molecules are contained in a pore, there are relatively more "interior" SA molecules than "boundary" SA molecules which adjacently interact with ZIF pore surface; since the T_m depression is mainly due to those "boundary" molecules, reducing the effective surface-to-volume ratio in this way also tends to reduce the T_m depression. The same principle holds for the ZIF-11 with the larger pore size which means the smaller surface-to-volume ratio.

We can also imagine a thought experiment with a phase change material that *repulsively* interacts with ZIF-11. If a few molecules of the phase change material are encapsulated in the ZIF-11 pore, they will now cluster at the center of pore (rather than being attracted to the pore walls as in the present study). This cluster could make a crystal structure with a *higher* phase change temperature because the surrounding potential field hinders the breaking and movement of the cluster. This kind of phase change temperature rise due to nano-confinement has been reported elsewhere.[40] Therefore, we conclude that the impact of attractive potential field from ZIF surface is the most critical factor to the number and strength of hydrogen bonds among SA molecules, and then consequentially results in the T_m depression. The nano-confinement strengthens the effect.

The effect from the attractive potential field of ZIF surface can be probed through the ratio between two directional movements, $2\langle dr^2(t_s)\rangle/\langle ds^2(t_s)\rangle$. This ratio reflects the degree of the weaker effect of the ZIF surface, and so approaches to 0 if the surface attractive interaction is

very strong and must equal 1 for pure bulk erythritol. We focus on times $t_s \geq t_{col}$ (where $t_s \geq 1.0$ ps). For all T, the results in Fig. 5 show that this ratio increases for the cases with more erythritol in a pore, for example compare $2\langle dr^2(t_s)\rangle/\langle ds^2(t_s)\rangle$ for Fig. 5a and Fig 5b. The ratio is also increasing towards 1 in the ZIF-11 as compared to ZIF-8 (compare top and bottom rows) which also makes sense because the ZIF-11 has a larger pore volume, in other words, the surface effect weakens and the SA experiences a more bulk-like environment overall.

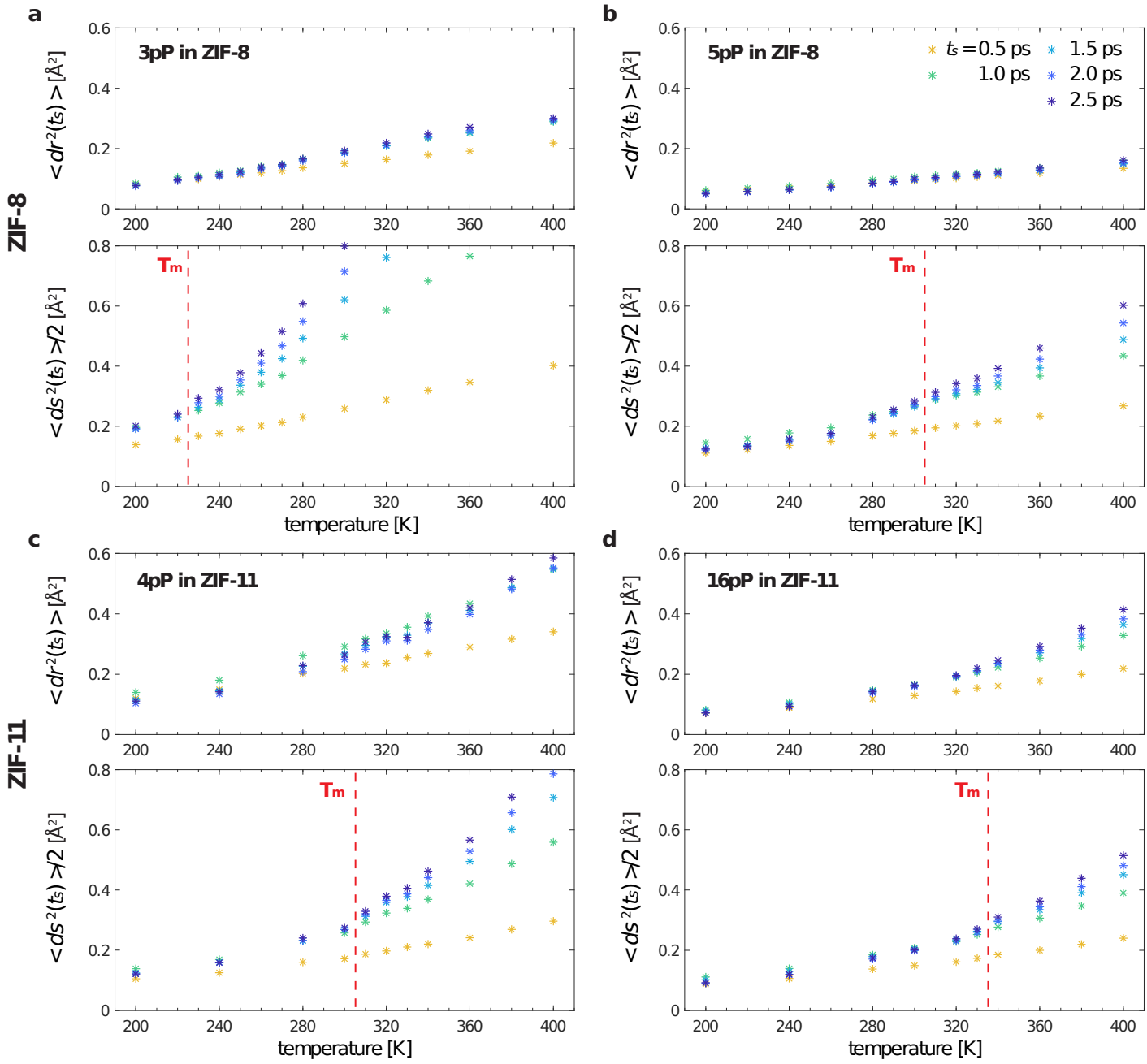

Figure 5. Mean squared displacements of encapsulated erythritol as a function of temperature, evaluated at the 5 different sampling times listed in panel (b,top). We decompose these displacements into the radial direction (dr^2; upper plot in each pair) and along the surface of the ZIF's approximately-spherical pore (ds^2; lower plot in each pair), as indicated in Fig. 4b. (a) 3pP in ZIF-8. (b) 5 pP in ZIF-8. (c) 4 pP in ZIF-11. (d) 16 pP in ZIF-11. In each case the melting temperature, T_m, is determined and indicated by a vertical red dashed line. For each sample, we define its T_m such that for all $T<T_m$ the ds^2 data is practically independent of t_s for 1.0 ps$\leq t_s \leq$2.5 ps, while for all $T>T_m$ the ds^2 data increases significantly with increasing $t_s \geq$1.0 ps.

Thermal conductivity

The thermal conductivity, *k*, of the pristine ZIFs and the composites with encapsulated erythritol is predicted by Green-Kubo method.[41] The GK method has been used to investigate the thermal properties of dielectric materials, and recently for MOFs.[42, 43] Since both ZIF-8 and ZIF-11 have cubic symmetry, their *k* is isotropic, which the GK method calculates as

$$k = \frac{1}{3 k_B T^2 V} \int_0^\infty \left\langle \vec{J}(0) \cdot \vec{J}(t) \right\rangle dt , \tag{4}$$

where k_B is the Boltzmann constant, V is the system volume, $\vec{J}(t)$ is the heat current, and $\left\langle \vec{J}(0) \cdot \vec{J}(t) \right\rangle$ is the heat current autocorrelation function (HCACF). The heat current is given by

$$\vec{J}(t) = \frac{d}{dt} \sum_i^N r_i E_i \tag{5}$$

where r_i and E_i are the position and total energy of particle *i*.

In this thermal conductivity investigation, we applied a shorter timestep, 0.5 fs. To prevent a divergence issue caused by a longer phonon lifetime at low temperatures, we prepared a larger simulation size with a 2x3x4 supercell for the pristine ZIF-8 and its composite cases, and a 1x2x3 supercell for the pristine ZIF-11 and its composite cases. This larger supercell sizes are also considered to make the size effect of simulation box size practically negligible.[42] The system is run first in an NPT and then NVT ensemble to set the temperature and volume. After the system has reached equilibrium, the heat current is obtained from runs in an NVE ensemble over 4 ns, then the thermal conductivity is obtained from the integral of the HCACF. For good convergence, every successive 10 ps of heat current data is treated as a different independent sample of the HCACF for use in Eq. (4). A running average is applied to define a convergence region,[42] then the thermal conductivity reaches a constant value at around 8 ps (Fig. S4). At each temperature and case, at least three independent runs are performed, and the averaged value is considered for the following discussion.

Figure 6 presents the result of this thermal conductivity calculation for pristine ZIF-8, pristine ZIF-11, and their composites with various numbers of erythritol molecules inside their pores. For context, a previous MD study with the Green-Kubo method had predicted the thermal conductivity of pristine (empty pores) ZIF-8 at 300 K and 1 bar as 0.165 $Wm^{-1}K^{-1}$,[43] which was the same order of magnitude as an experimental measurement[23] of in-air thermal conductivity of a ZIF-8 thin-film, 0.326 $Wm^{-1}K^{-1}$. The applied force field with DDEC6 partial charge in the present study predicts the thermal conductivity of pristine (empty pores) ZIF-8 at 300 K and 1 atm as 0.206 $Wm^{-1}K^{-1}$ which is somewhat closer to the experimental value. For the thermal conductivity of ZIF-11, this is the first calculation to the best of our best knowledge. The thermal conductivity of pristine ZIF-11 at the standard 1 atm and 300 K is predicted as 0.123 ± 0.004 $Wm^{-1}K^{-1}$ which is approximately half that of ZIF-8. The lower thermal conductivity of ZIF-11 could be problematic for transferring heat to and from the SAs inside their pores and become a barrier for practical thermal applications.

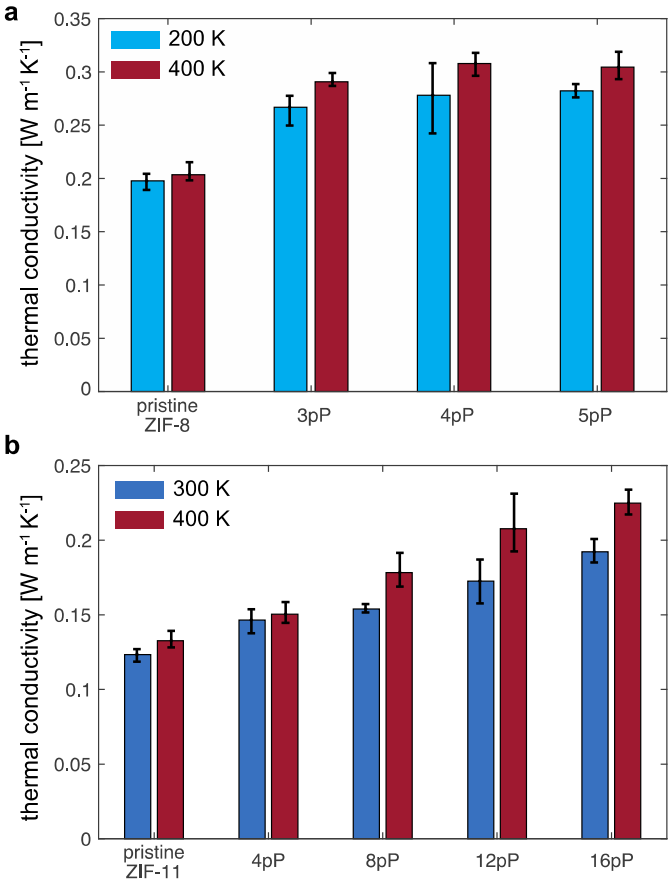

Figure 6. Thermal conductivity of pristine ZIFs and their composites with encapsulated erythritols. (a) ZIF-8 and its composites. (b) ZIF-11 and its composites. In each panel the cold and hot temperatures were chosen to ensure that the erythritol acts fully solid-like and liquid-like, respectively. Error bars show the maximum and minimum values from repeated calculations.

In order to investigate the influence of SA molecules on the thermal conductivity of the ZIFs, we calculate the thermal conductivities of composites by increasing the number of erythritol molecules in each pore. The results in Fig. 6 show that increasing the number of encapsulated erythritol molecules enhances the thermal conductivity for the both ZIF structures. This indicates that the erythritol molecules inside ZIF pores contribute to the heat transfer as additional parallel pathways. Note that fundamentally this increase was not a given, as the presence of additives in porous materials can positively or negatively affect the thermal conductivity of composites as new heat pathways or phonon scattering sources, respectively.[26]

The enhanced thermal conductivity at ZIF-11 composites is more sensitive in response to the number of erythritol molecules inside ZIF pores than at ZIF-8 composites. ZIF-11 has twice as large of an internal cavity distance in each pore compared to ZIF-8 (~20 Å vs 10 Å, as depicted in Fig. 2c and 2f). A single erythritol molecule effectively bridges end-to-end for the smaller pore, i.e. ZIF-8. Thus, in ZIF-8 a smaller number of erythritol molecules per pore is needed to fill up the vacant pore space and to enhance the thermal conductivity of composites. On the other hand, ZIF-11 has larger pores and thus requires more SA molecules per pore to effectively fill up the pores and create additional continuous heat flow pathways.

To elucidate further the thermal conductivity enhancement induced by the SA molecules, we perform a phonon frequency analysis on ZIF structures with and without SA molecules.[26, 43] The Fourier transform of the normalized HCACF, $\langle \vec{J}(0)\cdot\vec{J}(t)\rangle / \langle \vec{J}(0)\cdot\vec{J}(0)\rangle$, is used for the analysis as shown in Figs. 7a to 7c. The presence of SAs inside the ZIF pore does not disturb the major phonon frequency peaks of pristine ZIFs (compare the blue and red lines in Figs. 7a and b). Still, for both ZIFs the composite's peaks are stronger for frequencies around 40 THz, as seen in the insets. As seen in Fig. 7c this frequency range originates from the erythritol's

major phonon frequency for the amorphous liquid state, as highlighted with orange color in Figs 7a to 7c.

The ZIF-8 composite shows an additionally enhanced peak at a very low-frequency range (< ~2 THz; blue shading in Fig. 7b inset), which has long lifetimes. To understand the origin of the phononic heat transfer of the very low-frequency range, the vibrational density of states (VDOS) is calculated by taking the Fourier transform the atomic velocity autocorrelation function (VACF),[44]

$$VDOS(\nu)=\int \gamma(t)\exp(-2\pi j\nu)\,dt, \tag{6}$$

where ν is frequency, j is the imaginary number, and γ is the VACF which is defined as $\gamma(t)=\left\langle \sum_i v_i(0)\cdot v_i(t)\right\rangle / \left\langle \sum_i v_i(0)\cdot v_i(0)\right\rangle$. Figure 7d presents the VDOS for the atoms which are most important for energy transfer in ZIF-8,[43] namely Zn, N, and C1, as well as the VDOS for the edge atoms of erythritol, namely O, HO, and HC (details of labelling in Table S3). The O atoms in erythritol vibrate with the low-frequency phonon modes (< ~2 THz; blue shading in Fig. 7d) which overlap with the phonon modes of the main channel for energy transfer of ZIF-8 structure, Zn and C1. The 40 THz region phonon mode from erythritol is the major phonon mode of the edge hydrogen atoms (HO and HC, yellow shading) which closely interact with the ZIF ligands.

We also want to bring attention to the fact that the k of the liquid-like phase is larger than that of the solid-like phase, $k_{liquid\text{-}like} > k_{solid\text{-}like}$ seen in Fig. 6. This trend between solid-like vs. liquid-like erythritol is unusual compared to pure erythritol (0.89 ± 0.06 $Wm^{-1}K^{-1}$ at 20 °C solid and 0.33 ± 0.02 $Wm^{-1}K^{-1}$ at 140 °C liquid),[30] and most natural materials, which have $k_{liquid} < k_{solid}$.[45] To try to understand this unusual trend, we recall that Fig. 5 showed that the liquid-like SAs inside nanopores are more mobile than the solid-like SAs. At the atomistic scale within the framework structure, even at the highest SA loading conditions considered, there should be some vacant volume inside the pore which is not occupied by the SA molecules. Thus, a further heat

transfer can be induced by the direct SA molecules transport or a thermocapillary mechanism within the mobile liquid-like phase.

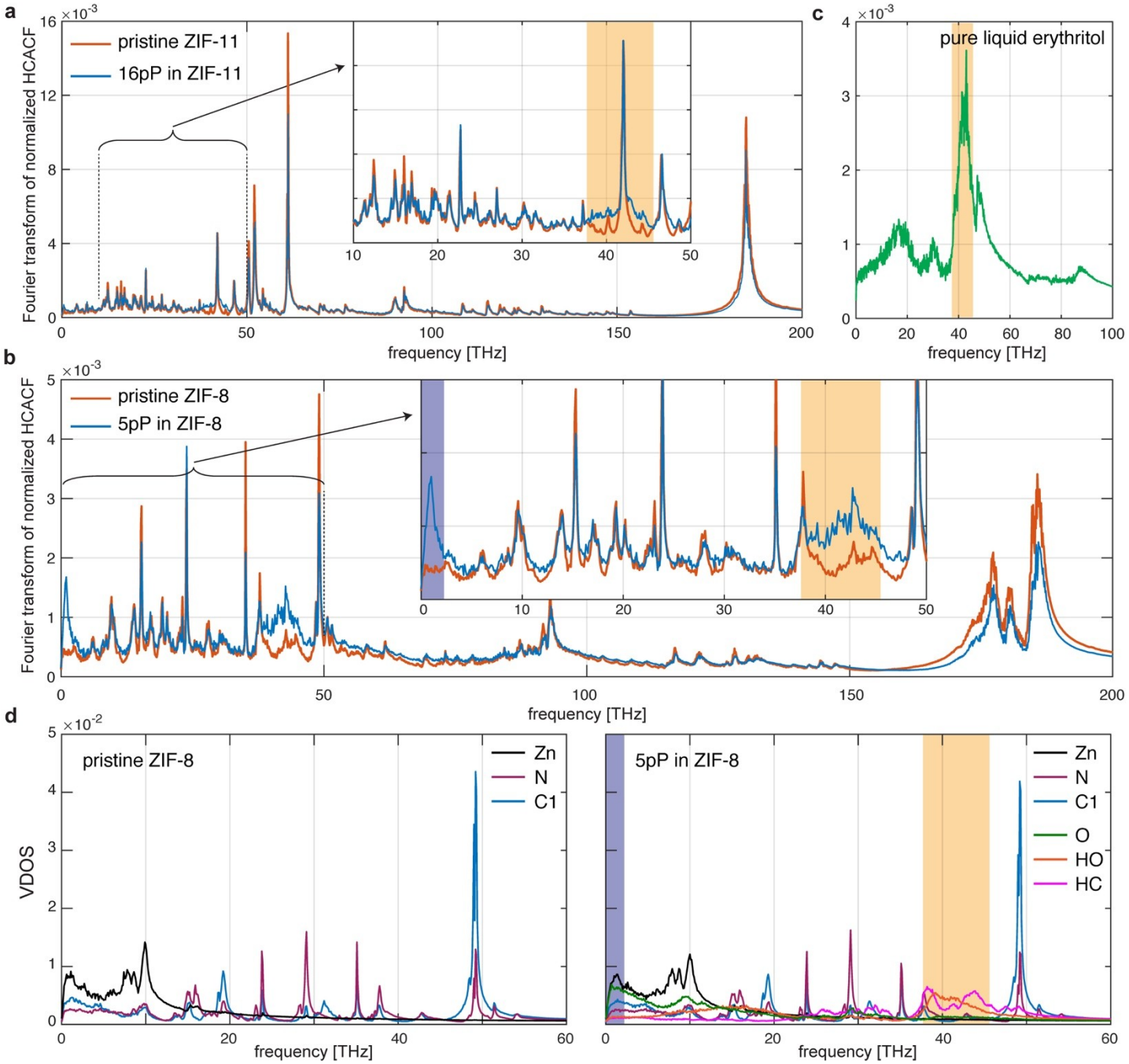

Figure 7. Phonon analysis by Fourier transform of the normalized HCACF and VACF at 400 K. (a) Comparison between pristine ZIF-11 and the case of 16pP in ZIF-11. The inset shows the 10-50 THz range in more detail. (b) Comparison between pristine ZIF-8 and the case of 5pP in ZIF-

8. (c) Pure liquid erythritol. (d) VDOS comparison between pristine ZIF-8 (left) and the case of 5pP in ZIF-8 (right). Shaded bands indicate the enhanced heat transfer originating from the contributions of the edge atoms of erythritol, namely O (<2 THz, blue shading) and HO & HC (~40 THz, yellow shading).

Conclusion

The amorphous phases of nanoconfined erythritol, as a representative of SAs, in ZIF-8 and ZIF-11 pores have been investigated by MD simulations. According to the structural analysis of ZIFs upon adding SAs into their pores, we verified the attractive interaction between ZIF structure and SA molecules by observing the reduced lattice constant in SA-loaded ZIF structures, and also confirmed that the small inter-pore aperture diameter of the ZIFs does not allow the SA molecules to diffuse among pores. The boundary attractive interaction of SAs to the ZIFs frustrated the crystallization of SAs and let them retain an amorphous structure even at temperatures far below the bulk melting point of 391 K. The decreased energy difference for the second-order phase transition between amorphous phases decreased the melting temperature of erythritol. Here, we suggested a way to determine the phase transition temperature by using the MSD with the fixed sampling times, which showed how the melting temperature of the nanoconfined erythritol is reduced from 391 K to 330 K or even lower, depending on the ZIF pore size and the number of SA molecules. We also explored the thermal conductivity of the SA-in-ZIF composites. The phonon frequency analysis through the HCACF and VDOS verified that the presence of SA molecules enhances the heat transfer by adding additional heat pathways between the nanoporous structure of ZIFs.

Supporting Information

Force field parameters for MD simulations; Mean Squared Displacement (MSD) to check diffusion; Radial distribution function at possible hydrogen bonding pairs; Heat current autocorrelation function.

Acknowledgements

The work at the Molecular Foundry was supported by the Office of Science, Office of Basic Energy Sciences, at the U.S. Department of Energy (DOE), Contract No. DE-AC02-05CH11231. H. K. gratefully acknowledges financial support from Kwanjung Educational Foundation. C. D. acknowledges the support of the NSF, Award No. 2020842.

Competing interests

The authors declare that they have no competing interests.

References

1. Farid, M. M.; Khudhair, A. M.; Razack, S. A. K.; Al-Hallaj, S., A review on phase change energy storage: materials and applications. *Energy conversion and management* **2004,** *45* (9-10), 1597-1615.
2. Zhang, S.; Wang, Z., Thermodynamics behavior of phase change latent heat materials in micro-/nanoconfined spaces for thermal storage and applications. *Renewable and Sustainable Energy Reviews* **2018,** *82*, 2319-2331.
3. Aftab, W.; Huang, X.; Wu, W.; Liang, Z.; Mahmood, A.; Zou, R., Nanoconfined phase change materials for thermal energy applications. *Energy & Environmental Science* **2018,** *11* (6), 1392-1424.
4. Kenisarin, M.; Mahkamov, K., Solar energy storage using phase change materials. *Renewable and sustainable energy reviews* **2007,** *11* (9), 1913-1965.
5. Lai, C.-C.; Chang, W.-C.; Hu, W.-L.; Wang, Z. M.; Lu, M.-C.; Chueh, Y.-L., A solar-thermal energy harvesting scheme: enhanced heat capacity of molten HITEC salt mixed with Sn/SiO x core–shell nanoparticles. *Nanoscale* **2014,** *6* (9), 4555-4559.
6. Yamagishi, Y.; Takeuchi, H.; Pyatenko, A. T.; Kayukawa, N., Characteristics of microencapsulated PCM slurry as a heat-transfer fluid. *AichE journal* **1999,** *45* (4), 696-707.
7. Merlin, K.; Soto, J.; Delaunay, D.; Traonvouez, L., Industrial waste heat recovery using an enhanced conductivity latent heat thermal energy storage. *Applied energy* **2016,** *183*, 491-503.
8. Khateeb, S. A.; Amiruddin, S.; Farid, M.; Selman, J. R.; Al-Hallaj, S., Thermal management of Li-ion battery with phase change material for electric scooters: experimental validation. *Journal of Power Sources* **2005,** *142* (1-2), 345-353.
9. Barzin, R.; Chen, J. J.; Young, B. R.; Farid, M. M., Peak load shifting with energy storage and price-based control system. *Energy* **2015,** *92*, 505-514.
10. Memon, S. A., Phase change materials integrated in building walls: A state of the art review. *Renewable and sustainable energy reviews* **2014,** *31*, 870-906.
11. Skovajsa, J.; Koláček, M.; Zálešák, M., Phase change material based accumulation panels in combination with renewable energy sources and thermoelectric cooling. *Energies* **2017,** *10* (2), 152.
12. Hyun, D. C.; Levinson, N. S.; Jeong, U.; Xia, Y., Emerging applications of phase-change materials (PCMs): teaching an old dog new tricks. *Angewandte Chemie International Edition* **2014,** *53* (15), 3780-3795.
13. Solé, A.; Miró, L.; Barreneche, C.; Martorell, I.; Cabeza, L. F., Corrosion of metals and salt hydrates used for thermochemical energy storage. *Renewable Energy* **2015,** *75*, 519-523.
14. Nomura, T.; Zhu, C.; Sagara, A.; Okinaka, N.; Akiyama, T., Estimation of thermal endurance of multicomponent sugar alcohols as phase change materials. *Applied Thermal Engineering* **2015,** *75*, 481-486.
15. Li, H.; Eddaoudi, M.; O'Keeffe, M.; Yaghi, O. M., Design and synthesis of an exceptionally stable and highly porous metal-organic framework. *nature* **1999,** *402* (6759), 276-279.

16. Wang, C.; Feng, L.; Yang, H.; Xin, G.; Li, W.; Zheng, J.; Tian, W.; Li, X., Graphene oxide stabilized polyethylene glycol for heat storage. *Physical Chemistry Chemical Physics* **2012,** *14* (38), 13233-13238.
17. Uemura, T.; Yanai, N.; Watanabe, S.; Tanaka, H.; Numaguchi, R.; Miyahara, M. T.; Ohta, Y.; Nagaoka, M.; Kitagawa, S., Unveiling thermal transitions of polymers in subnanometre pores. *Nature communications* **2010,** *1* (1), 1-8.
18. Tang, J.; Yang, M.; Dong, W.; Yang, M.; Zhang, H.; Fan, S.; Wang, J.; Tan, L.; Wang, G., Highly porous carbons derived from MOFs for shape-stabilized phase change materials with high storage capacity and thermal conductivity. *RSC advances* **2016,** *6* (46), 40106-40114.
19. Hackl, L.; Hsu, C.-H.; Gordon, M. P.; Chou, K.; Ma, C.; Kolaczkowski, M.; Anderson, C. L.; Liu, Y.-S.; Guo, J.; Ercius, P.; Urban, J. J., Sugar-alcohol@ZIF nanocomposites display suppressed phase-change temperatures. *Journal of Materials Chemistry A* **2020**.
20. Zhang, J.; Zhang, T.; Yu, D.; Xiao, K.; Hong, Y., Transition from ZIF-L-Co to ZIF-67: a new insight into the structural evolution of zeolitic imidazolate frameworks (ZIFs) in aqueous systems. *CrystEngComm* **2015,** *17* (43), 8212-8215.
21. Fu, H.; Wang, Z.; Wang, X.; Wang, P.; Wang, C.-C., Formation mechanism of rod-like ZIF-L and fast phase transformation from ZIF-L to ZIF-8 with morphology changes controlled by polyvinylpyrrolidone and ethanol. *CrystEngComm* **2018,** *20* (11), 1473-1477.
22. Park, K. S.; Ni, Z.; Côté, A. P.; Choi, J. Y.; Huang, R.; Uribe-Romo, F. J.; Chae, H. K.; O'Keeffe, M.; Yaghi, O. M., Exceptional chemical and thermal stability of zeolitic imidazolate frameworks. *Proceedings of the National Academy of Sciences* **2006,** *103* (27), 10186-10191.
23. Cui, B.; Audu, C. O.; Liao, Y.; Nguyen, S. T.; Farha, O. K.; Hupp, J. T.; Grayson, M., Thermal conductivity of zif-8 thin-film under ambient gas pressure. *ACS applied materials & interfaces* **2017,** *9* (34), 28139-28143.
24. McGaughey, A.; Kaviany, M., Thermal conductivity decomposition and analysis using molecular dynamics simulations: Part II. Complex silica structures. *International Journal of Heat and Mass Transfer* **2004,** *47* (8-9), 1799-1816.
25. Lee, S.-M.; Cahill, D. G., Heat transport in thin dielectric films. *Journal of applied physics* **1997,** *81* (6), 2590-2595.
26. Babaei, H.; DeCoster, M. E.; Jeong, M.; Hassan, Z. M.; Islamoglu, T.; Baumgart, H.; McGaughey, A. J.; Redel, E.; Farha, O. K.; Hopkins, P. E., Observation of reduced thermal conductivity in a metal-organic framework due to the presence of adsorbates. *Nature Communications* **2020,** *11* (1), 1-8.
27. Zheng, B.; Sant, M.; Demontis, P.; Suffritti, G. B., Force field for molecular dynamics computations in flexible ZIF-8 framework. *The Journal of Physical Chemistry C* **2012,** *116* (1), 933-938.
28. Manz, T. A.; Limas, N. G., Introducing DDEC6 atomic population analysis: part 1. Charge partitioning theory and methodology. *RSC advances* **2016,** *6* (53), 47771-47801.
29. Inagaki, T.; Ishida, T., Computational analysis of sugar alcohols as phase-change material: insight into the molecular mechanism of thermal energy storage. *The Journal of Physical Chemistry C* **2016,** *120* (15), 7903-7915.
30. Höhlein, S.; König-Haagen, A.; Brüggemann, D., Thermophysical characterization of

MgCl2· 6H2O, xylitol and erythritol as phase change materials (PCM) for latent heat thermal energy storage (LHTES). *Materials* **2017,** *10* (4), 444.
31. Plimpton, S., Fast parallel algorithms for short-range molecular dynamics. *Journal of computational physics* **1995,** *117* (1), 1-19.
32. https://lammps.sandia.gov/
33. Cornell, W. D.; Cieplak, P.; Bayly, C. I.; Gould, I. R.; Merz, K. M.; Ferguson, D. M.; Spellmeyer, D. C.; Fox, T.; Caldwell, J. W.; Kollman, P. A., A second generation force field for the simulation of proteins, nucleic acids, and organic molecules. *Journal of the American Chemical Society* **1995,** *117* (19), 5179-5197.
34. Liu, Z.; Huang, S.; Wang, W., A refined force field for molecular simulation of imidazolium-based ionic liquids. *The Journal of Physical Chemistry B* **2004,** *108* (34), 12978-12989.
35. Shinoda, W.; Shiga, M.; Mikami, M., Rapid estimation of elastic constants by molecular dynamics simulation under constant stress. *Physical Review B* **2004,** *69* (13), 134103.
36. Zhou, W.; Wu, H.; Udovic, T. J.; Rush, J. J.; Yildirim, T., Quasi-free methyl rotation in zeolitic imidazolate framework-8. *The Journal of Physical Chemistry A* **2008,** *112* (49), 12602-12606.
37. Moggach, S. A.; Bennett, T. D.; Cheetham, A. K., The Effect of Pressure on ZIF-8: Increasing Pore Size with Pressure and the Formation of a High-Pressure Phase at 1.47 GPa. *Angewandte Chemie International Edition* **2009,** *48* (38), 7087-7089.
38. Sapnik, A. F.; Geddes, H. S.; Reynolds, E. M.; Yeung, H. H.-M.; Goodwin, A. L., Compositional inhomogeneity and tuneable thermal expansion in mixed-metal ZIF-8 analogues. *Chemical Communications* **2018,** *54* (69), 9651-9654.
39. Zhang, Y.; Maginn, E. J., A comparison of methods for melting point calculation using molecular dynamics simulations. *The Journal of chemical physics* **2012,** *136* (14), 144116.
40. Zhang, S.; Wang, S.; Zhang, J.; Jiang, Y.; Ji, Q.; Zhang, Z.; Wang, Z., Increasing phase change latent heat of stearic acid via nanocapsule interface confinement. *The Journal of Physical Chemistry C* **2013,** *117* (44), 23412-23417.
41. McQuarrie, D., Statistical mechanics university science books. *Sausalito, CA* **2000**, 222-223.
42. Huang, B.; McGaughey, A.; Kaviany, M., Thermal conductivity of metal-organic framework 5 (MOF-5): Part I. Molecular dynamics simulations. *International journal of heat and mass transfer* **2007,** *50* (3-4), 393-404.
43. Zhang, X.; Jiang, J., Thermal conductivity of zeolitic imidazolate framework-8: A molecular simulation study. *The Journal of Physical Chemistry C* **2013,** *117* (36), 18441-18447.
44. Dickey, J.; Paskin, A., Computer simulation of the lattice dynamics of solids. *Physical Review* **1969,** *188* (3), 1407.
45. Hahn, D. W.; Özisik, M. N., *Heat conduction*. John Wiley & Sons: 2012.

TOC Graphic

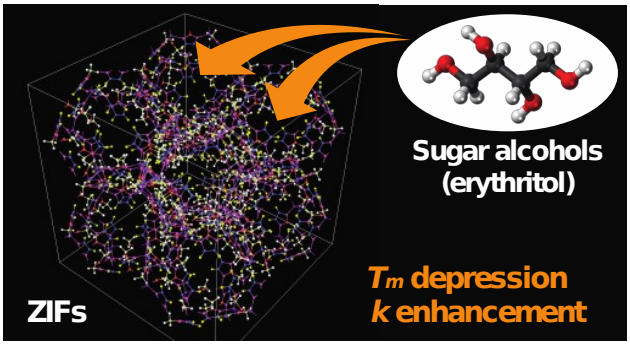
Sugar alcohols
(erythritol)
ZIFs
T_m depression
k enhancement